PCCP

Accepted Manuscript

This is an *Accepted Manuscript*, which has been through the Royal Society of Chemistry peer review process and has been accepted for publication.

Accepted Manuscripts are published online shortly after acceptance, before technical editing, formatting and proof reading. Using this free service, authors can make their results available to the community, in citable form, before we publish the edited article. We will replace this *Accepted Manuscript* with the edited and formatted *Advance Article* as soon as it is available.

You can find more information about *Accepted Manuscripts* in the **Information for Authors**.

ROYAL SOCIETY OF CHEMISTRY

www.rsc.org/pccp

Complex doping chemistry owing to Mn incorporation in

nanocrystalline anatase TiO$_2$ powders

Meilan Guo,[a,b] Yun Gao[b*] and G. Shao[a,c*]

[a] *Institute for renewable energy and environmental technologies, University of Bolton, Bolton, BL3 5AB, UK*

[b] *Faculty of Materials Science and Engineering, Hubei University, Wuhan, 430062, China*

[c] *UK-China Centre for Multifunctional Nanomaterials, Zhengzhou University, Henan, 450001, China*

Abstract: Mn-doped TiO$_2$ powders with a wide range of nominal doping levels were fabricated using a one-step hydrothermal method followed by 400℃ annealing. Anatase powders with a uniform size distribution below 10 nm were obtained. The maximum solubility of Mn in TiO$_2$ lattice was around 30%, beyond which Mn$_3$O$_4$ compound appeared as a secondary phase. The optical absorption edges for Mn-doped anatase TiO$_2$ were red-shifted effectively through increasing Mn content. Alloying chemistry and associated elemental valences were elaborated through combining X-ray photoelectron spectroscopy (XPS), X-ray absorption spectroscopy (XAS), and theoretical simulation in the framework of the density functional theory (DFT). The results showed that the Mn species exhibited mixed valence states of 3+ and 4+ in anatase TiO$_2$, with the latter being the key to remarkable photocatalytic performance.

[*]Corresponding author emails: gs6@bolton.ac.uk (GS); gaoyun@hubu.edu.cn (YG)

1 Introduction

As highly attractive multi-functional semiconductors, TiO_2 phases have attracted extensive attention owing to their great potential for applications in photonic devices, solar cells and photo-catalysis.[1-10] However, there is a critical barrier against effective exploitation of TiO_2 phases for many of such functional applications, since their wide energy band gaps (3.2 eV for anatase and 3.0 eV for rutile) lead to rather low utilization of the solar light within the ultra violet (UV) region. Enormous efforts have, therefore, been made towards reducing the band gaps of TiO_2 phases in order to extend their optical absorption edges into the visible range of the solar irradiance and thus enable their wide range of functionalities associated with quantum absorption of photons.[1-8] Naturally, incorporation of impurity species into the TiO_2 phases (i.e. doping or alloying) is widely accepted as an effective and feasible way to widen the optical absorption range of the solar irradiance.[9-14]

Numerous researchers have undertaken work on TiO_2 doping or alloying with non-metallic species (e.g. S, F, N, C),[1, 2, 4, 6, 15-17] or metallic elements (e.g. Fe, Co, Cu, V, Ga), [3, 8, 13, 18-22] either through experimental investigation or theoretical simulation (For the sake of simplicity in description, here in the paper we refer the incorporation of impurity element/species in the host phase as doping). Chemically, a non-metallic species tends to exist in the host metal oxide as an anion and metallic atoms present as cations. Great advancements have been made for anion doping of TiO_2, though significant difficulties have been experienced for effective incorporation of non-metallic species due to complexity in process control (e.g. anion-doping by flame pyrolysis).[1, 2, 6, 10, 12] Apart from anion doping, cation addition with transition metals is considered to be a promising means for effective doping. Among various transition metals (TM), variable-valence dopants such as Mn and Fe have been demonstrated to enhance absorption of the visible light.[9, 15, 18, 22] Our recent theoretical studies showed that the incorporation of Mn in rutile TiO_2 matrix induces significant modification of the electronic band structure, resulting in curvy intermediate bands within a shrinking forbidden gap.[19, 20] Such curvy intermediate bands (IB) can function effectively as stepping-stones to relay electrons from the valence band for multi-wavelength absorption of light and thus result in remarkable redshift for optical absorption well into the infrared region. It was encouraging that such theoretical predictions on the Mn-doped rutile phase were experimentally verified within our group, thus offering promising candidates for effective harvest of solar energy through remarkably extended optical absorption.[9] Owing to similar Mn effect on the electronic structure of the anatase phase, remarkable redshift was also achieved in Mn-doped anatase TiO_2 using a two-step sol gel method, which offers a highly potent system of photo-catalytic materials.[18]

Recent theoretical and experimental work showed that Mn doping leads to significant redshift in the optical gaps of TiO_2 phases, with the chemical states of Mn being associated with local structural configurations as well as structural defects depending on how Mn is incorporated in the host lattice.[8, 9, 18, 20] There exist, however, considerable discrepancies in reported experimental data and associated interpretation about Mn valences in doped TiO_2 materials.[18-20] This is partly due to the complexity associated with Mn being able to exhibit various valences in natural oxides, i.e. Mn^{2+}, Mn^{3+} and Mn^{4+}, and partly due to the uncertainty experienced in de-convolution of binding-energy peaks in experimental spectra from X-ray photoelectron spectroscopy (XPS), which is the main method in studying alloying chemistry.

Apparently, such uncertainty in identifying the doping chemistry associated with Mn incorporation makes it hard to study the functional effects, and hence hinders delivering effective doping processes to enable useful properties.

In line with recent advancement in high-coherence and high-intensity X-ray sources from modern synchrotron facilities, X-ray absorption spectroscopy (XAS), particularly spectroscopic analysis for the X-ray near-edge structure (XANES), is becoming a more and more powerful tool for studying alloying/doing chemistry owing to its unique advantage in revealing "fingerprints" of chemical states and local electronic structure of incorporated atoms in the host compounds even at a dilute concentration.[23-25] With currently achievable high resolution and high signal-to-noise ratio, XAS provides a powerful means for studying chemical states associated with local structural and electron orbital environments such as shown in distinguishing species of the same oxidation state but different local structures (e.g. Ti^{4+} in [TiO4] and [TiO6]), which is impossible for XPS.[26-28] Elaborating information owing to crystal field of different ligands is a significant advantage of XAS and a dramatic dependence on local environment can be revealed from XANES spectra.[26, 29-30] It is thus expected that through combining XANES and XPS analyses, one would be able to achieve reliable and self-consistent interpretation of the role of the dopants in a host matrix.

Theoretical simulation in the framework of the density functional theory (DFT) are known to be a powerful means for predicting and interpreting the electronic structures of materials such as doped TiO_2 with respect to structural and chemical changes.[19, 20, 31, 32] Recently, DFT modelling with the consideration of non-local contribution to the exchange-correlation (XC) functionals has been successfully applied to study the electronic structures and associated functional properties of various transition metal oxides. The core-level DFT calculations can be used to predict binding spectra corresponding to XAS or electron energy loss spectroscopy (EELS), as both XAS and EELS follow the same principles in gathering binding information owing to quantum excitation of core-level electrons.[24, 29, 33-35] For example, theoretically predicted EELS spectra for the rutile and anatase phases of the pristine TiO_2 phases were in good agreement with experimental spectra,[5, 35] and the results proved that XAS or EELS is highly sensitive to structural/chemical configurations in the near edge structures, and is thus indeed able to provide "fingerprint" information for alloying chemistry.

In this work, we aim at a systematic study of alloying/doping chemistry owing to the incorporation of different levels of Mn into the anatase TiO_2 nano-crystalline powders, which were synthesized by a new one-step hydrothermal method. Through complementary use of XPS and XAS, together with DFT simulation, we focus on reliable identification of Mn valences, which are essential for the doping induced functionalities such as photonic properties and photocatalysis. The experimental Ti and Mn *2p* XPS and XANES spectra were used to probe the doping effects via associated valence states, owing to their impact on the electronic structure of Mn-doped anatase TiO_2. DFT simulation was carried out to assist interpreting the experimental XAS data, thus enabling self-consistent deconvolution of the XPS spectra for reliable assignment of the valence states to chemical species in the materials. Correlation of alloying chemistry to photocatalytic activity, on elimination of a model dye for waste organics, suggests that the Mn^{4+} cations are most potent on decomposing organic wastes.

2 Experimental Methods

2.1 Materials synthesis

Pure and doped TiO_2 powders were fabricated by a one-step hydrothermal method adapted from a recent sol gel method,[18] using the framework linking the two techniques presented in our recent work.[21] All chemicals used for material synthesis were of Analytical Reagent (AR) grade. Tetrabutyl titanate (TBOT) and manganese nitrate $Mn(NO_3)_2$ were chosen as Ti and Mn sources respectively, with $Mn(NO_3)_2$ having been diluted with ethanol in advance.

During a typical hydrothermal process, 10 mL TBOT was added drop by drop into a mixture of 37.5 mL ethanol and 1.5 mL deionized water in a glass beaker with continuous stirring at a moderate speed. Certain amount of HNO_3 was used to control the concentration of H^+ to 0.735M. And different amounts of $Mn(NO_3)_2$ was then added to the mixture according to different nominal doping levels to prepare the precursor sols. Each sol was then transferred to a Teflon container in a sealed stainless autoclave, to conduct the reaction at 160 ºC for 12 hours. After naturally cooling down to the ambient temperature, the sample was taken out and washed by distilled water until it was neutralized, and then dried in air. In order to reduce defects in the materials, all the powder samples were annealed in air at 400 ºC for 1h. In order to study the Mn content on doping chemistry, powders with a series of nominal atomic doping levels (Mn/Ti), 0%, 1%, 2%, 5%, 12%, 20%, 30%, 50% were synthesized, which are referred here as M0, M1, M2, M5, M12, M20 and M50 correspondingly.

2.2 Materials characterization

X-ray diffraction (XRD) was employed to examine the crystal structures of the powders using a Bruker D8 Discover diffractometer. Microstructural study was carried out using transmission electron microscopy (TEM, FEI Tecnai TF20) and energy-dispersive X-ray (EDX, Oxford Instruments INCA 350 EDX system) spectroscopy. Optical absorbance of the samples was measured using a UV-vis spectrometer (Shimadzu UV-VIS-NIR 3600) equipped with an integrating sphere (ISR-2200).

The chemical states of metallic elements were analysed by X-ray photoelectron spectroscopy (XPS, Thermo Scientific ESCALAB250), with a monochromatic Al Ka X-ray source (photon energy hυ = 1486.6 eV) radiation operated at 150 W with a spot size of ~500 μm. The analytical chamber was maintained at 2×10^{-9} Torr. Survey spectra and high-resolution spectra were recorded in the fixed analyzer transmission mode with pass energy of 150 eV and 10 eV respectively. The overlapped XPS peaks were deconvoluted and fitted with Gaussian peaks after subtraction of a Shirley background. The spectrometer was calibrated using the C 1s peak at 284.6 eV. On the basis of data from instrumental calibration, an error below 0.3 eV could be considered for all the measurements.

The Ti and Mn L-edge XANES spectra were recorded at the Shanghai Synchrotron Radiation Facility (SSRF) Centre (3.5 GeV storage ring), being operated at a current in the range between 200 and 300 mA. The total electron yield (TEY) mode with a good signal-to-noise ratio was used for both Ti and Mn spectra in the soft X-ray beam line BLO8U-1A. This beam line was monochromatised over an energy range 250 - 2000 eV to deliver 2×10^7 photos per second. The beam size residing on the samples was 100μm×100μm

and the vacuum was maintained at 10^{-5} Torr to avoid absorption of air. The neutralization current yield at the sample holder was monitored through an ammeter.

Each powder sample was evenly spread on a piece of conductive copper tape immediately prior to X-ray absorption spectroscopy (XAS). A coarse scan was carried out initially for each measurement to check that alignment for maximum energy flux was achieved and a refined scan was then followed. Parameters such as slit size, step size, dwell time, and count of spectra for each statistical analysis were carefully examined. An optimal test condition (slit size $100\mu m \times 100\mu m$, step size 0.2 eV, dwell time 0.1, count 10) was chosen to maintain adequate signal-to-noise ratio without prolonged radiation to avoid sample damage.[23] Each sample was measured for 3 times on different positions. All XANES spectra were normalized against incident intensity (I_0), which was measured simultaneously by current yield.

2.3 Photocatalytic activity

Evaluation of photo-activity of Mn-doped TiO_2 was conducted under visible-light irradiation using a high-pressure mercury lamp as light source through a long-pass filter with a cutoff of 420 nm to remove the near-UV portion of high-energy photons. The measurement was conducted in a cylindrical Pyrex vessel surrounded by a water-cooling jacket with magnet stirring. The methylene blue (MB) was chosen as a model degrading dye to test the photocatalytic activity for decomposing organic wastes.

The MB solution for catalytic assessment was prepared by dispersing 1g of Mn-doped TiO_2 in 50ml of MB aqueous solution (8 mg/L). Absorption–desorption equilibrium was achieved before subjecting the solution to light irradiation. A sample of 3 ml solution was taken from the photo-reactor every 45 min during the course of experiment, which was centrifuged to remove TiO_2 particles. The concentration of MB was determined by the change in the optical absorbance at 662 nm (Shimadzu UV-VIS-NIR 3600), which corresponded to the wavelength with maximum optical absorption for MB.

2.4 Theoretical modelling

First principle modelling in the framework of the density functional theory (DFT), using the well-tested CASTEP code, was carried out to predict electronic structures and optical absorption spectra of Mn-doped anatase, with a Mn atom to substitute a Ti atom in anatase supercells. Details for DFT parameters suitable to TiO_2 were based on extensive tests carried out in recent work.[19, 20] The exchange functional by Wu and Cohen was used together with the PBE description of the correlation functional (PBE-WC) to describe the General Gradient Approximated (GGA) for the exchange-correlation (XC) functional. It is known that the GGA functional determined by the local electron density and its gradient is inadequate to predict the band structures of correlated systems such as transition metal oxides. The nonlocal part of XC was considered by the inclusion of an effective Hubbard U parameter of 7 eV to account for the on site coulomb interaction between d electrons.[20, 36] The energy cutoff for the plane wave basis set was kept at 400 eV throughout the calculations. The reciprocal space sampling was decided with k-point Monckhorst-Pack, with k point spacing being maintained not to be more than 0.04 Å^{-1}. The tolerance for accepting convergence of a single eigenvalue per band during band structure calculation is set to be 1×10^{-5} eV. In addition to calculation of optical

properties and band structures, DFT simulation of core-level spectroscopy was carried out to assist interpreting the near edge fine structures of the experimental XAS spectra at the Mn $2p$ edges.

3. Results and Discussion

3.1 Crystal structures

XRD patterns of synthesized powder samples are presented in **Fig. 1**(a), wherein patterns from different samples are normalised to the intensity of the (101) peak for anatase TiO_2. The lower panels are standard powder patterns for anatase and Mn_3O_4. All diffraction peaks including relative intensities from samples doped up to 30% Mn/Ti agree excellently well with the standard powder pattern for anatase TiO_2 (PDF NO. 89-4921). While it is known that Mn incorporation assists phase transition from the anatase structure into the rutile phase,[5, 9] the current observation that high levels of Mn were retained in an anatase host. This is consistent with the finding that anatase formation is promoted through using oxidic acids such as HNO_3 and H_2SO_4, [21, 37-39] to adjust PH to lower acidic levels. A lower acidity destabilises the prior solution and quickens precipitation through enhanced condensation and associated crystal growth kinetics, which in turn favours the formation of zigzagging Ti-O-Ti bonds characteristic of the anatase structure.[21, 37] It is reasonable to envisage that fast precipitation kinetics helps the anatase phase to gobble doping elements while growing, thus enhancing metastable solubility of doping/alloying elements such as Mn.

In addition to anatase peaks, four additional minor peaks situated at 29°, 36.09°, 32.54° and 60° appeared in the powder with high Mn content (M50). Referring to the standard pattern in the lowest panels, one can see that these peaks are consistent with the strong diffraction lines of Mn_3O_4.[40-41] This is in line with the fact that there is a solid solubility threshold for Mn incorporated into TiO_2 lattices, with the excess Mn species forced into the as-synthesised materials being rejected from the host during annealing.[42]

It is worth pointing out that the position of (004) peak from the anatase phase shifted towards higher diffraction angle (2θ) with increasing doping levels (**Fig. 1**(b)), while the (101) peak at lower angle experienced little shift. This indicates a lattice contraction along the c-axis due to the addition of Mn, which is in agreement with previous reports on Mn-doped TiO_2 films and powders.[36, 42,43] As indicated by the arrow in **Fig. 1**(b), the (004) peak from M50 shifts backwards with respect to that from M30. This is attributable to the precipitation of Mn_3O_4, hence decreasing Mn content towards a significantly lowered level.[12, 36, 42, 44]

One notices that Mn incorporation in the anatase phase led to some peak broadening. For example, distinguishable peaks in the middle of the pattern from the M0 and M1 powder samples (at around 55°) were seen to merge in samples of higher Mn contents. The grain size in Mn-doped TiO_2 samples is estimated by applying the Scherrer formula to the strongest (101) peak, Fig. 1(c), which shows that incorporation of Mn led to reduction in average grain size, from about 10 nm in the pristine powder to about 5 nm in the M50 sample, being in agreement with previous observations.[21, 43, 45]

TEM from the powder samples confirmed the grain sizes derived from the XRD data. For example, a high-resolution TEM (HRTEM) image from the M20 sample is shown in **Fig. 2**(b), revealing anatase nanocrystals about 6 nm in size. The selected area diffraction from the

M20 powers, **Fig. 2(a)**, only contained diffraction rings from the anatase phase, supporting the XRD outcome. The fast Fourier transform (FFT) image from the indicated nanocrystal in **Fig. 2(b)** corresponds to the [010] zone axis of the anatase phase. Regions oriented off low-index zone axes were beyond the resolution limit of the microscope and thus could not be resolved in the HRTEM image.

EDX measured Mn/Ti ratios in the powders are compared with nominal compositions in **Fig. 3**, showing a positive correlation between the nominal and actual compositions. One notes that overall it became more difficult in incorporating Mn in the TiO_2 host in samples with increasing nominal Mn level in the reactants, and the highest Mn/Ti level achievable was about 35% for M50 (well below the nominal 50%). Similar actual Mn/Ti ratios were achieved in M30 and M50, indicating approaching a solubility limit associated with the near-equilibrium hydrothermal process in this work, with the host anatase phase being unable to contain Mn levels as high as those reported in far-from-equilibrium processes such as magnetron sputtering deposited rutile films.[9]

The variation in the level of Mn incorporation was also revealed in the optical absorption spectra. **Fig. 4** shows the effect of Mn content on the UV-Vis absorbance derived from the diffuse reflectance spectra. With respect to the sharp absorption edge at about 400 nm for the pure TiO_2 powder, Mn incorporation was seen to induce remarkable redshift in optical absorption, which is in line with previous reports on TiO_2 phases.[9, 13, 18, 21]

3.2 Doping chemistry in Mn-doped TiO_2 powders

High-resolution X-ray photoelectron spectroscopy was carried out to study the Mn effect on the chemical states of the constituent elements in TiO_2 powders. Ti $2p$ core level XPS of Mn-doped TiO_2 powders at various doping levels are shown in **Fig. 5**, with all spectra exhibiting the spin-orbit doublet peaks of Ti $2p_{3/2}$ and Ti $2p_{1/2}$. The peaks are of excellent symmetry with similar half peak width, or the full width at half peak maximum (FWHM). For M1 with rather low Mn content, the peaks at 458.2 and 464.0, with a peak separation of 5.8 eV (vs. the reported 5.67 eV), can be assigned to Ti^{4+} (TiO_2), being in excellent agreement with reported data[9, 14, 18, 22, 44, 46-53], through the consideration of the discrepancy in the position of the C 1s peak for spectrum calibration and as well as the instrumental error below 0.3 eV for XPS analysis. Peak shifting slightly larger than the nominal instrumental error (< 0.3 eV) towards lower binding energy is noticeable in powders of higher Mn contents (0.35 eV for M12, 0.3 eV for M20, 0.15 eV for M50). This may indicate slightly weakened binding due to the incorporation of considerable amount of Mn into the host anatase lattices of M12 and M20 samples.

Fig. 6(a) show Mn $2p$ peaks from doped TiO_2, which exhibits no XPS signals from metallic Mn (637.7 eV) in any of the samples.[44, 49] The peaks for all samples were asymmetric and broad, implying multi-valence states of Mn in TiO_2. In particular, the peaks of M12 and M20 showed considerable shifts towards higher energy (0.55 eV and 1.0 eV respectively), while little shift was observed from M50 (0.04 eV). The results showed that incorporation of Mn into the anatase phase enhanced binding of the Mn ions, being contrary to the effect on the binding of the Ti ions. The smaller shift in the Mn peaks, and as well as in the Ti peaks, for M50 corresponded to the fact that phase separation occurred in the annealed samples, which reduced the Mn content in anatase. Peak deconvolution showed multi-valence states of

Mn ions in these Mn-doped anatase powders. **Fig. 6**(b) and (c) show resultant peak fitting for samples M20 and M50, as examples. The outcomes for peak areas associated to different Mn valence states are summarised in **Table 1**.

Some discrepancies exist in reported peak positions of Mn ions with different valences,[27, 54-55] which is further complicated due to different chemical environments associated with the different data sources. Fundamentally Mn-O binding is somewhat weaker than the Ti-O binding due to different oxygen affinities,[9, 19, 20] and it is thus expected that introduction of some Mn ions into a Ti-O bond environment will weaken the overall Ti-O binding and strengthen the Mn-O binding. This means that the position of Mn or Ti peaks will be affected by the local atomic/ionic configuration, and it is thus rather challenging to determine the valences of metal ions from reported peak positions, which are often obtained from quite different compound structures. For example the binding energy for Mn^{4+} will be somewhat different in the TiO_2 lattices from that in the MnO_2 lattices.

On the basis of the recently established approach in modelling the Mn-doped TiO_2, we have calculated the theoretical valences of Mn in the TiO_2 lattices, and the results show that while Mn tends to assume a valence similar to that the host metal at low doping level, higher Mn incorporation leads to lowered valence, due to charge screening with Ti tending to pass some electrical charges towards Mn. Fundamentally, the higher the valence of a metal ion, the bigger is the binding energy, through charge transferring from metal to oxygen. The general trend for the binding energy of Mn ions with different valences, therefore, follows the sequence: $Mn^{4+} > Mn^{3+} > Mn^{2+}$. A summary of binding energies of Mn ions in TiO_2 was established on the basis of careful examination of published data, considering instrumental resolution, value of C 1s binding energy used for calibration and materials compositions/structures.[9]

The Mn 2p peaks become more asymmetrical with increasing amount of Mn incorporation, indicating the existence of significant amount of multi-valences. **Fig. 6**(b) presents the resultant peak deconvolution for M20 as an example, with one set of Mn 2p peaks sitting at 641.6 and 653.2 and the other set sitting at higher energies 643.3 and 654.6. These two sets of peaks are assigned to the Mn^{3+} and Mn^{4+} states respectively.[9, 18, 22, 44, 33] For samples with even higher Mn content, e.g. M50, in addition to these two sets of Mn 2p peaks, another set of peaks appears at 640.0 eV and 651.5 eV, which needs to be assigned to a lower valence of Mn^{2+}. This is consistent with the existence of Mn_3O_4 (see XRD results). It is worth pointing out that the binding energy for the 2p peaks of the Mn^{4+} states in the TiO_2 powders are lower than the reported binding energy,[9, 27, 54] which is attributed to difference in structural configuration and local chemical environment of Mn^{4+} ions in the TiO_2 host.

Table 1 lists the percentages of peak areas derived from XPS results, showing a general trend for enhanced lower valence states with increasing amount of Mn addition. For the M50 sample, which contained Mn_3O_4, an additional set of Mn 2p peaks corresponding to Mn^{2+} are present. This is consistent with the well-recognised fact that Mn_3O_4 consists of both 3+ and 2+ valence states, with the ratio of Mn^{3+}/Mn^{2+} from experiments lying between 1.5 and 2.6 (2 is the theoretical value for the bulk Hausmannite manganese oxide).[34, 40-41, 56-57] The percentage of the Mn^{4+} peak area decreases from M1 to M50, which is consistent with DFT prediction that increased Mn at the metal sites leads to lowered valence of Mn ions. On the basis of areas, *we have the area ratio Mn^{3+}/Mn^{2+} ~1.9 for M50, which is in the range of*

reported values for Mn_3O_4. Some Mn^{3+} and especially Mn^{4+} in M50 are owing to Mn remained in the host of TiO_2 phase. Even in samples of low Mn contents, e.g. M1, the average of Mn valences was still lower than 4+. The finding that Mn valences lower than 4+ are present in the Mn-containing TiO_2 powder is consistent with the theoretical finding that there is a tendency for Ti atoms to pass some charges to the nearby Mn, as the latter has lower oxygen affinity.[19-20] Also, the presence of lower oxidation state of Mn can arise from Mn being incorporated at defective sites (e.g. interstitial position) or in the vicinity of defects (e.g. oxygen vacancy) [9], and to reduce such defects, annealing at 400 ^{o}C for 1h was carried out for all the powder samples in this work. While it is rather difficult to quantify the amount of such structural defects and their contribution towards the overall Mn^{2+} valence, one is aware that higher Mn content is associated with larger defect density due to the metastable nature for their incorporation in the anatase host. As the Mn^{2+} valence was only shown in the M50 powder, when the precipitation of Mn_3O_4 contributed to lower the Mn content in the anatase host even lower than that of the M12 and M20 powders, we can conclude that the main contribution to the Mn^{2+} oxidation state in Table 1 is from the Mn_3O_4 phase. This is supported by the fact that our measured areal ratio Mn^{3+}/Mn^{2+} ~1.9 for M50 is well within the reported range for Mn_3O_4 (1.5 − 2.6).[34, 40-41, 56-57]

In order to eliminate possible uncertainty due to interpretation of XPS results based on peak fitting, we also carried out X-ray absorption spectroscopy to register spectra for both Ti ($3d^2 4s^2$) and Mn ($3d^5 4s^2$) L-edges, as XANES spectra often carry fingerprint information sensitive to both valence and local structural configuration (e.g. Ti in anatase and rutile can be readily differentiated[28, 58]). The high-resolution XANES results are presented in **Fig. 7**. Each Ti L-edge XANES spectrum from the powder samples of this work, **Fig. 7** (a), consists of two sets of peaks at 455 - 461 eV and 462 - 470 eV, corresponding to the L_3 and L_2 edges. Being typical to XAS, peaks appear at lower energy are of better resolution. All spectra are aligned at 458.2 eV,[28, 52, 58] marked as the c peak in the L_3 edge in **Fig. 7**(a). There is ignorable difference in the Ti L-edges from powder samples of different Mn contents. The energetic separation between L_2 and L_3 edges for all spectra is 5.3 eV, which agrees well with reported energy change owing to the $2p_{1/2}$ and $2p_{3/2}$ spin-orbit splitting from XPS analysis.[52, 58-60] Such an energetic splitting is mainly attributed to the transition from the *2p* core orbital to unfilled *3d* orbital in the conduction band, together with minor contribution from the *2p* to *4s* transition.[23, 59] While the intensity ratio of L_3 and L_2 is about 2:1 in principle for XPS, the area ratio of L_3 and L_2 edges for XAS was found to deviate somewhat from 2:1 even for pure *3d* metals,[59-62] with the ratio being also dependent on material systems.[23] In this work, the integral TEY intensity ratios obtained after a background subtraction are 2.3 for pure powder (M0), and 2.1 after doping with Mn. The origin for such edge ratio discrepancy between XPS and XAS was discussed by de Groot and co-workers,[60, 62] with the consideration of the initial state d spin-orbit coupling and the overlap between the 2p wave function and the 3d wave functions, due to the so called "multiple effects". Some researchers also considered the correlation effect to play an important role in XAS results.[58-63] Two minor pre-edge peaks (indicated as a and b) can be seen in the XAS spectra from all samples, which were attributed to multiplet core hole interaction with d electrons in precious reports.[28, 52, 58]

Additional splitting observed within L_2 and L_3 regions respectively is primarily attributed to the effect of crystal field of oxygen ligand associated with the t_{2g} and e_g symmetry of the *3d*

orbitals (peaks c and d/e, and f and g).[52, 59, 62-63] Within the Ti L_3 edge, the e_g-related peak is further split into two peaks, labelled d and e. As was reported in references 57 and 58, the intensity ratio of peak d and e for Ti^{4+} is reversed between the anatase and rutile phases, while for the Ti^{3+} oxidation state, the intensity of peak d and e are the same. On the basis of such "fingerprint" features of the fine structures within the Ti L_3 edge, we can conclude that Ti in all the powder samples of interest to this work existed in the anatase phase, with the Ti^{4+} valence state, which is in agreement with the XRD results.

Coming back to XPS analysis of Ti in the powders, one finds that it is extremely difficult to determine the valence state of Ti in the oxide powders of interest, as the reported peak positions Ti^{3+} (457.8 eV for Ti_2O_3) is extremely close to that of the Ti^{4+} (458.2 eV for TiO_2) and the binding energy for Ti^{4+} alone can vary from 458.1 eV to 459.2 eV (Ti 2p3/2).[9, 18, 47-48] The relative intensity between the d and e peaks in the XANES of the Ti edge, on the other hand, provides strong evidence that no Ti^{3+} existed in the samples, and the observed slight shift in the XPS spectra is indeed solely attributed to reduced binding due to Mn incorporation.

The XANES results from the Mn L edge are presented in **Fig. 7**(b), with each spectrum exhibiting two groups of peaks with a spin-orbit separation around 11 eV.[9, 18, 23, 64] Compared to the L_2 edge, the L_3 edge on the left (637 – 647 eV) is of higher intensity with better energetic resolution. The measured intensity ratios of L_3/L_2 are found to decrease with increasing Mn contents. For example, the ratio for M5 (Mn/(Mn+Ti)=5.96% from EDX) is 3.1, and intensity ratios decreased significantly for samples with higher Mn contents (~2.1 for M12, 2.5 for M30 and 1.8 for M50). While the change in the intensity ratio can be attributed to the "multiple effects", the fundamental details remain to be elaborated. Unlike the XPS method, the XANES spectra are significantly sensitive to local chemical/structural configurations in samples. This makes it rather hard to interpret results on the basis of so-called standard peak positions and edge profiles derived from samples of rather different structures, even though such a method has been followed in many reports,[23, 30, 65-68] largely due to the lack of fundamental understanding. In particular, it is reasonable to expect that the Mn L edge in a TiO_2 host would look rather different from those in pure Mn oxides, even when they are of the same valence states. This was demonstrated extensively in reference 58, for example, which showed the Ti^{4+} L edges are significantly different from TiO_2 of different structures.

Also, the L_3 edges (635 - 648 eV) for Mn in powder samples free of Mn oxides (M1 – M30) exhibit two peaks, with the relative intensity and width of the secondary peak being enlarged with increasing Mn content. It is shocking to note that the characteristics of observed Mn L_3 spectra in TiO_2 do not resemble any reported spectra from pure Mn oxides of different crystal structures from anatase, namely stable oxides such as MnO, Mn_2O_3, and MnO_2.[23, 30, 66] This suggests again that local structural configuration plays a remarkable role in the near edge fine structures. Mn XANES spectra from pure Mn_3O_4 powder were also collected to compare with that from the M50 sample, and there are rather similar features between the two spectra. This is consistent with the XRD results that phase separation occurred in M50 with the precipitation of Mn_3O_4 to take most Mn out of the TiO_2 lattice. On the basis of XPS observed peak shift, most Mn existed in the Mn_3O_4 precipitates. Overall, the M50 spectrum is dominated by the Mn_3O_4 feature, with some contribution of Mn in the TiO_2 host. This is also

consistent with our interpretation of the XPS results that multi-valence states of Mn existed in the M50 sample.

The fundamental basis in the near edge structure for XAS is the same as that for electron energy loss spectroscopy (EELS).[34, 52, 56, 67] Recent advancement in theoretical modelling based on the density functional theory (DFT) enables one to simulate EELS or XANES spectra with well-defined local structural configurations [69]. The effect on Mn content on the L_3 spectra Mn in TiO_2 could be simulated by substituting a Ti with Mn in an anatase supercell containing different numbers of TiO_2 unit cells. On the basis of well-tested parameterisation for DFT modelling of Mn-doped TiO_2 system [20], we have calculated the near edge structure for Mn L_3 spectra, and the results are summarised in **Fig. 7**(c). The MnO_2 phase referred in **Fig. 7**(c) is of the anatase structure. One can see that the characteristic features of calculated spectra compare well with the observed splitting in the L_3 edge, in the presence of a major peak and a secondary peak next to it on the right. The Mn content on the metallic sublattice sites increases in the hypothetical supercell structures of the anatase phase in the order of 3x3x1 (2.78% Mn), 2x2x1 (6.25% Mn), 1x1x1 (25% Mn) and anatase-structured MnO_2 (100% Mn). Being in agreement with the experimental spectra, the DFT results show that increased Mn content leads to enhancement and broadening in the secondary peak. Interestingly, even in the case of complete replacement of Ti by Mn, the main peak is still higher than the secondary ones in the form of a plateau. The simulated results are therefore in agreement with our experimental observation, such that higher Mn content leads to enhanced secondary peak in the L_3 spectra of Mn. Also, for MnO_2 in the hypothetical anatase structure, the calculated spectrum is drastically different from the experimental spectrum recorded from the stable MnO_2 oxide, which is attributed to remarkable structural difference from the stable MnO_2 phase.[56, 67, 70] Indeed, the near edge structure of XAS or EELS spectrum is so sensitive to local structural configurations, that recent EELS analysis showed that the L_3 edge for Cu collected from within a CuO crystal or from grain boundaries showed some different features.[71] Ahmad et al. demonstrated by theoretical simulation that even for an element of the same valence, variation of local structural configuration could induce significant difference in EELS spectra,[71] thus offering fundamental insight for the interpretation of experimental EELS evidence as presented by Tan et al.[34] It is therefore evident that the relative peak intensities in XANES or EELS are highly informative of the local structural/chemical configuration, even though spectroscope calibration for XAS or EELS is less accurate than for XPS. Such sensitivity in local structure in XANES or EELS suggests rather a different approach in interpreting experimental XAS/EELS spectra from that of XPS. With the assistance of both experimental standard and simulated XANES for the L edge of Mn in the anatase structure, we are able to conclude with confidence that the Mn in the M50 powder does exist mainly in the Mn_4O_3 compound. It would be interesting to extend the XANES study to the K edge for Mn, which would help to shed light upon the effect of chemical bonding on core-level orbitals well below the valence band.

Our results in this work help to highlight the following fact not yet well realised for spectroscopy study of chemical bonding: unlike the XPS method that is largely dictated by core level energy, spectra obtained from different structures cannot be used to assist interpretation of XANES/EELS spectra due to the importance of local structure and associated valence band. For the same reason, there is no straightforward way to determine

the chemical valence of elements from the XAS or EELS measurement, and one then needs to rely on theoretical simulation to derive such data. On the basis of Mulliken charge analysis,[9] we can calculate the normalised charge of Mn. Using the supercell structural models, we find that the valence of Mn decreases with increasing Mn content on the metal sites. The corresponding valence of Mn in the 3x3x2 (1.39% Mn), 2x2x2 (3.36% Mn), and 2x2x1 (6.25% Mn) supercells are 3.37+, 3.28+, and 3.06+, with increasing Mn leading to lower valence. The highest average valence for Mn achieved in this work was 3.4 (derived from **Table 1**), being consistent with theoretical prediction.

3.3 Effect on electronic structure

High-resolution valence band XPS (VBXPS) were used to assess the Mn effect on total occupied density of states around the Fermi energy, with typical results summarised in **Fig. 8**. The valence bandwidth of $\sim$ 6.7 eV for M1 is in excellent agreement with the reported experimental width for pure anatase,[73-74] slightly larger than theoretical value from the calculated density of states (DOS).[32, 74] Overall, Mn incorporation led to elevation of the valence band maximum (VBM) to lower binding energy, and as well as broadening of the valence band, which is similar to the case of Mn-doped rutile phase.[9]

Electronic structure of Mn-doped TiO_2 are calculated using the DFT+U method, with details on modelling parameters given in recent work.[9, 20] **Fig. 9** shows typical band structure and partial density of states by substituting a Ti atom with Mn in a 2x2x1 anatase supercell, with reference to the 0 K Fermi energy at 0 eV. The results for the Mn effect on anatase are strikingly similar to those for Mn-doped rutile, in that Mn substitution of Ti atoms leads to two curvy intermediate bands (IB) within the forbidden gap, due to interaction between the oxygen $2p$ and Mn $3d$ orbitals.[19, 20] Similar to the case of Mn-doped rutile phase, Mn-O interaction in the anatase phase also induces spin polarisation. The existence of the Mn-induced intermediate bands (IBs) leads to division of the forbidden gap into two effective sub-gaps, with the lower sub-gap smaller than the upper one (0.93 eV vs. 1.04 eV). The narrower lower gap is associated with higher probability for exciting valence electrons to the IBs, with the IBs acting as a crowded temporary host for excited electrons waiting to be pumped up to the CB under further excitation. This makes the wider upper sub-gap the bottleneck for optical absorption through a relaying process using the IBs as a step stone for photo excited hole-electron pairs.[20] It is worth pointing out that IBs within the forbidden gap can also play a role for inter-band recombination. The advantage for the curvy IBs induced by Mn doping implies good mobility for charge carriers associated with them. This in turn suggests that excited carriers within them are rather mobile and they do not have to be trapped there waiting for recombination to happen, before playing a role in useful functionality such as photo-catalysis or photovoltaics. The uplifting of VBM owing to the incorporation of Mn is also consistent with the VBXPS results.

It is widely recognised that the presence of IBs within the forbidden gap of a semiconductor material leads to redshift in the optical absorption edge. Optical properties originate from the interaction of photons with the electrons in a system, which can be described in terms of time-dependent perturbations of the ground state electronic states. Transitions between occupied and unoccupied states are caused by the electric field of each photon. When the transitions are independent they are known as single particle excitations,

and the spectra owing to these excitations can be considered as a joint density of states between the valence and conduction bands, weighted by appropriate matrix elements to introduce selection rules. The widely used CASTEP code on DFT modelling of condensed matter treats such single-particle excitations to calculate the dielectric properties of condensed phases,[69] and application of this method to the rutile Mn-doped rutile TiO_2 led to excellent agreement with experimental observations.[9] The optical properties were calculated using parameters justified in reference 20, using an effective Hubbard U parameter of 7 eV to account for the non-local effect in the exchange-correlation functional. The overall effect of substitutional Mn on the optical properties is shown in the calculated optical absorption spectra of Mn-doped anatase with different fraction of Ti replacement, **Fig. 10**. Apparently, the redshift in the optical edge is significant due to Mn incorporation. The presence of IBs is seen to lead to a secondary absorption shoulder, in addition to redshift in the primary optical edge. The lower optical absorption associated with the IBs correspond to their lower DOS. The tail structure in the calculated optical absorption spectrum for the virgin phase confirms the existence of lower indirect gap. The overall trend for optical redshift is consistent with the experimental observation, as shown in **Fig. 4**. Significant red-shift owing to Mn substitution of Ti leads to the effective optical absorption range of doped materials well into the infrared region of light, which is expected to bring about important impact for multi-functionalities associated with optical absorption and related electron-hole pairs generated. In particular, this is fundamental for enhanced photovoltaic effect or photo-catalytic properties.

The effect of Mn doping on photo-catalysis was demonstrated through the destruction of the benchmark organic dye, the methylene-blue under visible light. The results are summarised in **Fig. 11**. With respect to the effect of pure anatase powder, Mn-doping is seen to enhance photo-catalytic activity under visible light. The best photo-catalytic activity was achieved with the powder doped with 1% Mn, which contained the highest percentage of Mn^{4+} ions (**Table 1**). This is consistent with the observation in Mn-doped powder fabricated using a sol gel process.[18]

4. Conclusions

Mn-doped anatase TiO_2 powders with a wide range of nominal doping levels were fabricated using a one-step hydrothermal method followed by annealing at 400℃ to reduce defects. Mn-doped TiO_2 nanoparticles with a uniform size distribution below 10 nm were obtained. The maximum achievable solubility of Mn in TiO_2 lattice was around 35% in Mn/Ti ratio, beyond which precipitation of Mn_3O_4 occurred during annealing.

Complex chemical states of metal ions in the doped oxides were determined self-consistently through the combination of XPS and XAS methods, together with the assistance of DFT simulation for the interpretation of the results from the latter. While Ti in the doped powders maintained the 4+ valence state, Mn ions of lower than 4+ valences appeared, with percentage of lower valence states increasing with the Mn content.

Similar to its effect on rutile TiO_2, Mn-doping of anatase TiO_2 also induces intermediate bands within narrowed forbidden gap, which leads to remarkable redshift in optical absorption. Enhanced optical absorption is fundamental to enable a wide range of functionalities such as photovoltaic energy harvest and photocatalysis under visible light.

Mn incorporation results in remarkably improved photo-catalytic activity under visible

light, though the best performance is associated with the high valence Mn^{4+} ions.

References

1   S. U. M. Khan, M. Al-Shahry, W. B. Ingler Jr., *Science,* 2002, **297**, 2243.

2   X. Chen, L. Liu, P. Y. Yu, S. S. Mao, *Science,* 2011, **331**, 746.

3   K. Umar, M. M. Haque, M. Muneer, T. Harada, M. Matsumura, *J. Alloy. Compd.,* 2013, **578**, 431.

4   G. Liu, L. C. Yin, J. Wang, P. Niu, C. Zhen, Y. Xie, H. M. Cheng, *Energy Environ. Sci.,* 2012, **5**, 9603.

5   N. Vast, L. Reining, V. Olevano, P. Schattschneider, B. Jouffrey, *Phys. Rev. Lett.,* 2002, **88**, 037601.

6   T. Xia, X. Chen, *J. Mater. Chem. A,* 2013, **1**, 2983.

7   Z. Zhao, J. Tian, D. Wang, X. Kang, Y. Sang, H. Liu, J. Wang, S. Chen, R. I. Boughtond, H. Jiang, *J. Mater. Chem.,* 2012, **22**, 23395.

8   Q. Deng, X. Han, Y. Gao, G. Shao, *J. Appl. Phys.,* 2012, **112**, 013523.

9   X. H. Xia, L. Lu, A. S. Walton, M. Ward, X. P. Han, R. Brydson, J. K. Luo, G. Shao, *Acta Mater.,* 2012, **60**, 1974.

10   S. U. M. Khan, M. Al-Shahry, W. B. Ingler Jr., *Science,* 2003, **301**, 1673.

11   R. Zhang, Q. Wang, J. Liang, Q. Li, J. Dai, W. Li, *Physica B,* 2012, **407**, 2709.

12   X. Li, S. Wu, P. Hu, X. Xing, Y. Liu, Y. Yu, M. Yang, J. Lu, S. Li, W. Liu, *J. Appl. Phys.,* 2009, **106**, 043913.

13   S. Binghama, W. A. Daoud, *J. Mater. Chem.,* 2011, **21**, 2041.

14   P. Esparza, T. Hernández, M. E. Borges, M. C. Álvarez-Galván, J. C. Ruiz-Morales, J. L. G. Fierro, *Catal. Today,* 2013, **210**, 135.

15   N. R. Khalid, Z. Hong, E. Ahmed, Y. Zhang, H. Chana, M. Ahmad, *Appl. Surf. Sci.,* 2012, **258**, 5827.

16   J. Fu, Y. Tian, B. Chang, F. Xi, X. Dong, *J. Solid State Chem.,* 2013, **199**, 280.

17   X. Han, G. Shao, *J. Phys. Chem. C,* 2011, **115**, 8274.

18   Q. R. Deng, X. H. Xia, M. Guo, Y. Gao, G. Shao, *Mater. Lett.,* 2011, **65**, 2051.

19   G. Shao, *J. Phys. Chem. C,* 2008, **112**, 18677.

20   G. Shao, *J. Phys. Chem. C,* 2009, **113**, 6800.

21   L. Wan, Y. Gao, X. H. Xia, Q. R. Deng, G. Shao, *Mater. Res. Bull.,* 2011, **46**, 442.

22   C. Y. W. Lin, D. Channei, P. Koshy, A. Nakaruk, C. C. Sorrell, *Physica E,* 2012, **44**, 1969.

23   J. Kawai, Y. Mizutani, T. Sugimura, M. Sai, T. Higuchi, Y. Harada, Y. Ishiwata, A. Fukushima, M. Fujisawa et al., *Spectrochim. Acta B,* 2000, **55**, 1385.

24   S. M. Butorin, J. H. Guo, M. Magnuson, P. Kuiper, J. Nordgren, *Phys. Rev. B,* 1996, **54**, 4405.

25   R. J. Iwanowski, E. Welter, E. Janik, *Appl. Surf. Sci.,* 2008, **254**, 7183.

26   K. E. Lee, M. A. Gomez, T. Regier, Y. Hu, G. P. Demopoulos, *J. Phys. Chem. C,* 2011, **115**, 5692.

27   M. Oku, K. Wagatsuma, T. Konishi, *J. Electron Spectrosc.,* 1999, **98–99**, 277.

28   G. S. Henderson, X. Liu, M. E. Fleet, *Phys. Chem. Miner.,* 2002, **29**, 32.

29   A. L. Ankudinov, J. J. Rehr, *Phys. Rev. B,* 1997, **56**, 1712.

30   F. Morales, F. M. F. de Groot, P. Glatzel , E. Kleimenov, H. Bluhm, M. Hävecker, A. Knop-Gericke, B. M. Weckhuysen, *J. Phys. Chem. B,* 2004, **108**, 16201.

31   M. E. Arroyo-de Dompablo, A. M. García, M. Taravillo, *J. Chem. Phys.,* 2011, **135**, 054503.

32   D. O. Scanlon, C. W. Dunnill, J. Buckeridge, S. A. Shevlin, A. J. Logsdail, S. M. Woodley et al., *Nat. Mater.,* 2013, **12**, 798.

33   F. Morales, F. M. F. de Groot, O. L. J. Gijzeman, A. Mens, O. Stephan, B. M. Weckhuysen, *J. Catal.,* 2005, **230**, 301.

34   H. Tan, S. Turner, E. Yücelen, J. Verbeeck, G. Van Tendeloo, *Phys. Rev. Lett.,* 2011, **107**, 107602.

35   C. Heiliger, F. Heyroth, F. Syrowatka at al., *Phys. Rev. B,* 2006, **73**, 045129.

36   A. L. J. Pereira, L. Gracia, A. Beltrán, P. N. Lisboa-Filho, J. H. D. da Silva, J. Andrés, *J. Phys. Chem. C,* 2012, **116**, 8753.

37   M. Guo, X. Xia, Y. Gao, G. Jiang, Q. Deng, G. Shao, *Sensor. Actuat. B-Chem.,* 2012, **171-172**, 165.

38   Z. Wang, D. Xia, G. Chen, T. Yang, Y. Chen, *Mater. Chem. Phys.,* 2008, **111**, 313.

39   B. Tian, F. Chen, J. Zhang, M. Anpo, *J. Colloid. Interf. Sci.,* 2006, **303**, 142.

40   B. Gillot, M. El Guendouzi, M. Laarj, *Mater. Chem. Phys.,* 2001, **70**, 54.

41   D. P. Dubalz, D. S. Dhawale, R. R. Salunkhe, C. D. Lokhandez, *J. Electrochem. Soc.,* 2010, **157,** 812.

42   S. Sharma, S. Chaudhary, S. C. Kashyap, S. K. Sharma, *J. Appl. Phys.,* 2011, **109**, 083905.

43   D. Gautam, R. P. Chaudhary, *Spectrochim. Acta Part A,* 2012, **98**, 256.

44   X. Y. Li, J. R. Xiao, Z. Y. Wang, S.W. Li, *Mat. Sci. Eng. B – Solid,* 2012, **177**, 869.

45   C. Y. W. Lin, A. Nakaruk, C. C. Sorrell, *Prog. Org. Coat.,* 2012, **74**, 645.

46   S. K. Kim, G. J. Choi, S. Y. Lee, M. Seo, S. W. Lee, J. H. Han, H. S. Ahn, S. Han, C. S. Hwang, *Adv. Mater.,* 2008, **20**, 1429.

47   V. V. Atuchin, V. G. Kesler, N. V. Pervukhina, Z. Zhang, *J. Electron Spectrosc.,* 2006, **152**, 18.

48   J. T. Mayer, U. Diebold, T. E. Madey, E. Garfunkel, *J. Electron Spectrosc.,* 1995, **73**, 1.

49   M. Xue, L. Huang, J. Q. Wang, Y. Wang, L. Gao, J. Zhu, Z. G. Zou, *Nanotechnology,* 2008, **19**, 185604.

50   E. Park, H. Le, S. Chin, J. Kim, G. N. Bae, J. Jurng, *J. Porous Mater.,* 2012, **19**, 877.

51   Z. Wu, R. Jin, H. Wang, Y. Liu, *Catal. Commun.,* 2009, **10**, 935.

52   M. E. Fleet, S. L. Harmer, X. Liu, H. W. Nesbitt, *Surf. Sci.,* 2005, **584**, 133.

53   J. B. Yin, X. P. Zhao, *J. Phys. Chem. B,* 2006, **110**, 12916.

54   H. W. Nesbitt, D. Banerjee, *Am. Mineral.,* 1998, **83**, 305.

55   G. C. Allen, S. J. Harris, J. A. Jutson, J. M. Dyke, *Appl. Surf. Sci.,* 1989, **37**, 111.

56   L. Laffonta, P. Gibotb, *Mater. Charact.,* 2011, **61**, 1268.

57   J. A. Koza, I. P. Schroen, M. M. Willmering, J. A. Switzer, *Chem. Mater.,* 2014, **26**, 4425.

58   S. O. Kucheyev, T. van Buuren, T. F. Baumann, J. H. Satcher, T. M. Willey et al., *Phys. Rev. B,* 2004, **69**, 245102.

59   F. M. F. de Groot, J. C. Fuggle, B. T. Thole, G. A. Sawatzky, *Phys. Rev. B,* 1990, **42**, 5459.

60   F. M. F. de Groot, Z. W. Hu, M. F. Lopez, G. Kaindl, F. Guillot, M. Tronc, *J. Chem. Phys.,* 1994, **101**, 6570.

61   J. Fink, T. Müller-Heinzerling, B. Scheerer, W. Speier, F. U. Hillebrecht, J. C. Fuggle, J. Zaanen, G. A. Sawatzky, *Phys. Rev. B,* 1985, **32**, 4899.

62   F. M. F. de Groot, *Physica B,* 1995, **208-209**, 15.

63   L. D. Finkelstein, E. I. Zabolotzky, M. A. Korotin, S. N. Shamin, S. M. Butorin, E. Z. Kurmaev, J. Nordgren, *X-Ray Spectrom.,* 2002, **31**, 414.

64   M. M. Grush, J. Chen, T. L. Stemmler, S. J. George, C. Y. Ralston, R.T. Stibrany, A. Gelasco, G. Christou, S. M. Gorun, J. E. Penner-Hahn, S. P. Cramer, *J. Am. Chem. Soc.,* 1996, **118**, 65.

65   R. S. Liu, L. Y. Jang, J. M. Chen, J. B. Wu, R. G. Liu, J. G. Lin, C. Y. Huang, *Solid State Commun.,* 1998, **105**, 605.

66   K. P. K. Kumar, J. C. Jan, J. W. Chiou, H. M. Tsai, C. W. Bao, B. C. Hsu, D. C. Ling, W. F. Pong, M. H. Tsai, *J. Electron Spectrosc.,* 2005, **144-147**, 529.

67   R. S. Liu, J. B. Wu, C. Y. Chang, J. G. Lin, C. Y. Huang, J. M. Chen, R. G. Liu, *J. Solid State Chem.,* 1996, **125**, 112.

68   B. Gilbert, B. H. Frazer, A. Belz, P. G. Conrad, K. H. Nealson, D. Haskel, J. C. Lang, G. Srajer, G. De Stasio, J. Phys. Chem. A, 2003, 107, 2839.

69   S. J. Clark, M. D. Segall, C. J. Pickard, P. J. Hasnip, M. J. Probert, K. Refson, M. C. Payne, *Z. Kristallogr.* 2005, **220**, 567.

70   G. H. Du, Z. Y. Yuan, G. Van Tendeloo, Appl. Phys. Lett., 2005, **86**, 063113.

71   Y. Shen, M. Guo, X. Xia, G. Shao, Acta Mater., 2015, **85**, 122.

72   E. A. Ahmad, G. Mallia, D. Kramer, V. Tileli, A. R. Kucernak, N. M. Harrison, Phys. Rev. Lett., 2012, **108**, 259701.

73   G. Silversmit, G. De Doncker, R. De Gryse, Surf. Sci. Spectra, 2002, **9**, 21.

74   G. Liu, C. Sun, H. G. Yang, S. C. Smith, L. Wang, G. Lu, H. M. Cheng, *Chem. Commun.*, 2010, **46**, 755.

75   M. Landmann, E Rauls, W. G. Schmidt, *J. Phys. - Condens. Mat.*, 2012, **24**, 195503.

Figure captions:

Figure 1 (a) XRD patterns of Mn-TiO$_2$ powders with various doping concentrations. The bottom panel shows the standard XRD pattern of anatase TiO$_2$ and Mn$_3$O$_4$.   (b) Enlarged view of peak (004) to show corresponding peak shift. (c) Grain size estimated by applying the Scherer's formula to the (101) peak.

Figure 2 (a) SAED patterns and (b) HRTEM image from M20. The inset in (b) shows the corresponding FFT of indicated grain on the right.

Figure 3 EDX determined Mn/Ti ratios vs. nominal doping levels.

Figure 4 Diffuse reflection absorption spectrum of Mn-TiO$_2$ powders with different levels of Mn incorporation.

Figure 5 High-resolution XPS spectra of Ti 2p in samples of different Mn levels.

Figure 6 High-resolution XPS spectra of (a) Mn 2p. (b) Deconvoluted peaks of Mn 2p from (b) M12, and (c) M50.

Figure 7 (a) Ti $L_{3,2}$-edge and (b) Mn $L_{3,2}$-edge XANES spectra from Mn-TiO$_2$ with various doping levels. (c) Calculated EELS L_3 edge spectrum of Mn-TiO$_2$ with various doping levels with MnO$_2$ having the anatase structure.

Figure 8 VBXPS spectra of Mn-TiO$_2$ nanoparticles, with an arrow-headed line guiding the evident elevation in the VBM due to Mn doping. The right panel shows the near edge part of the spectra, with the edge positions indicated by the intercepts of the slopes on the energy axis.

Figure 9 Spin polarized band structures (left) and corresponding partial density of states (PDOS, right) for a 2×2×1 anatase supercell containing a substitutional Mn atom. The corresponding Mn/(Ti +Mn) is 6.25%.

Figure 10 DFT + U calculated optical spectra showing the effects of substitutional Mn doping. A Gaussian smearing of 0.5 eV is applied to account for a virtual instrumental resolution.

Figure 11 Photo-degradation of methylene blue by TiO$_2$ powder under visible light.

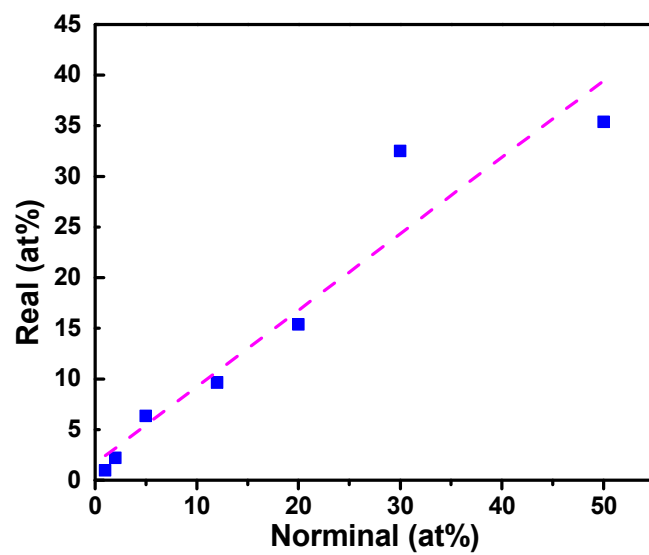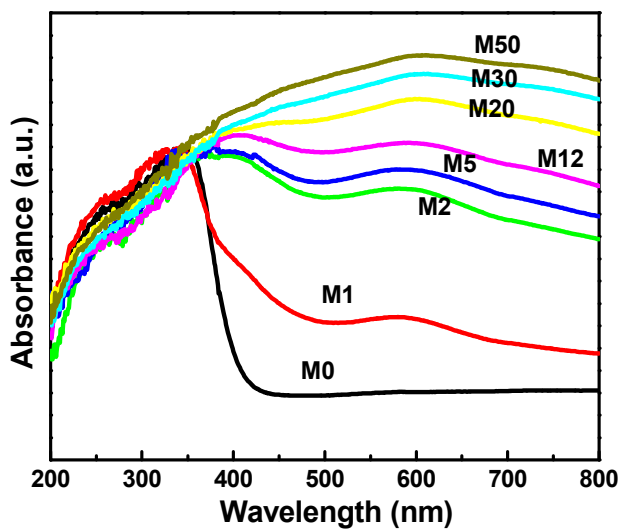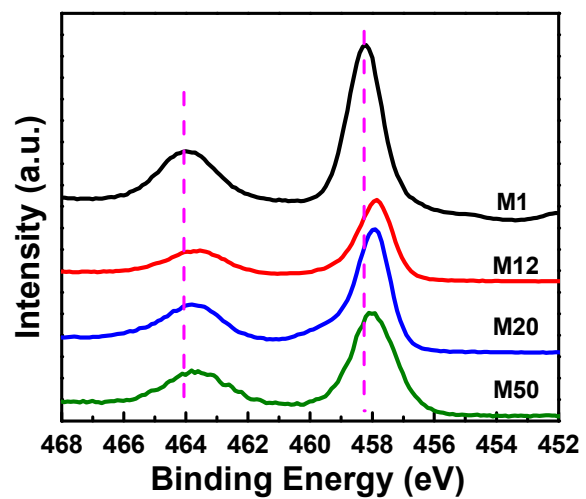**Table 1** Deconvoluted Ti *2p* and Mn *2p* peak areas in Mn-TiO$_2$. The atomic percentages are determined from EDX.

Sample	At.% Mn/Ti	At.% Mn/(Mn+Ti)	Peak area (%)/FWHM		
			Mn^{2+}	Mn^{3+}	Mn^{4+}
M1	1.0	1.0		59.6	40.4
M12	9.68	12.8		62.9	37.1
M20	16.77	15.6		73.4	26.6
M50	35.4	32.8	27.7	52.5	19.8
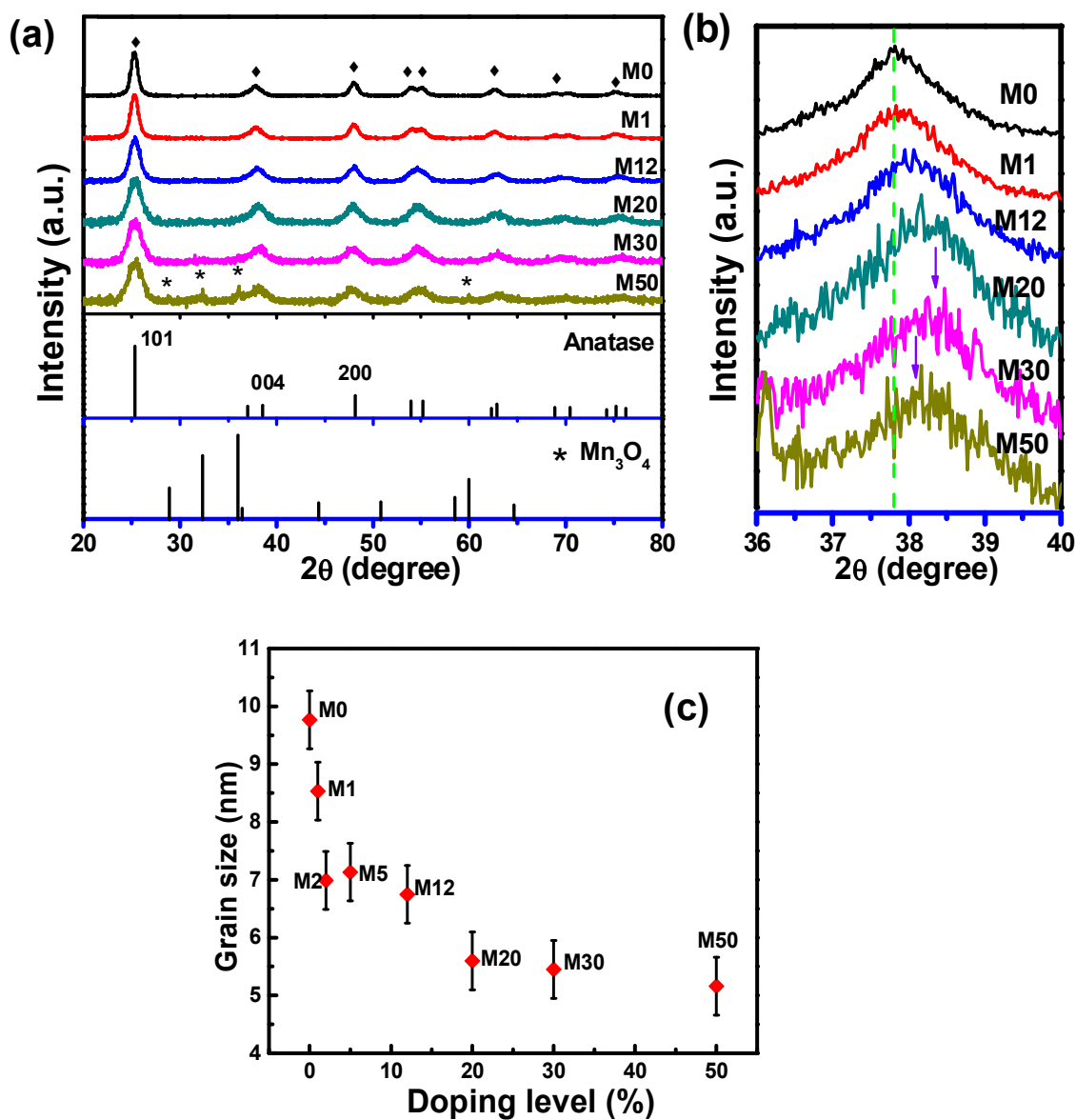
Figure 1 (a) XRD patterns of Mn-TiO$_2$ powders with various doping concentrations. The bottom panel shows the standard XRD pattern of anatase TiO$_2$ and Mn$_3$O$_4$. (b) Enlarged view of peak (004) to show corresponding peak shift. (c) Grain size estimated by applying the Scherer's formula to the (101) peak.
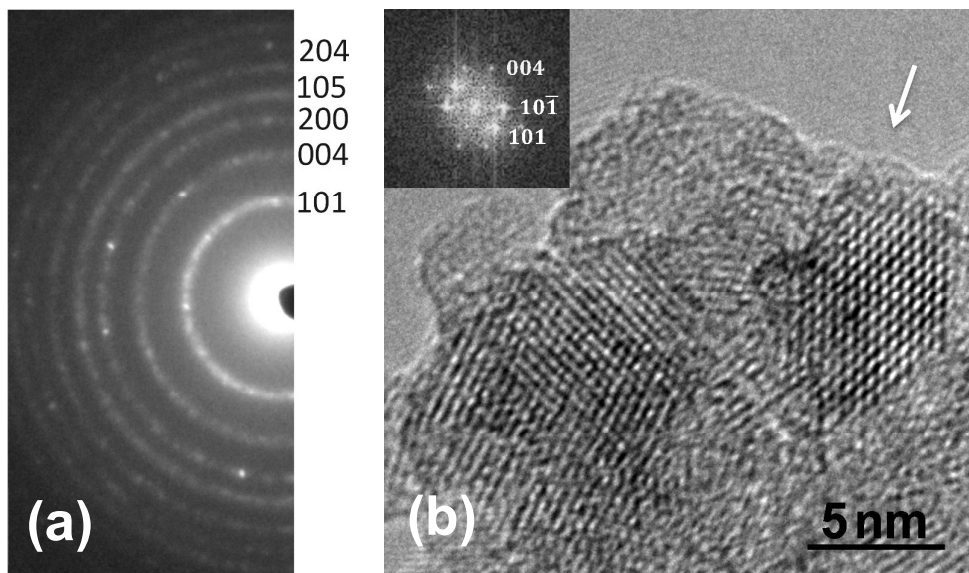
Figure 2 (a) SAED patterns and (b) HRTEM image from the M20 powder. The inset in (b) shows the corresponding FFT of indicated grain on the right.
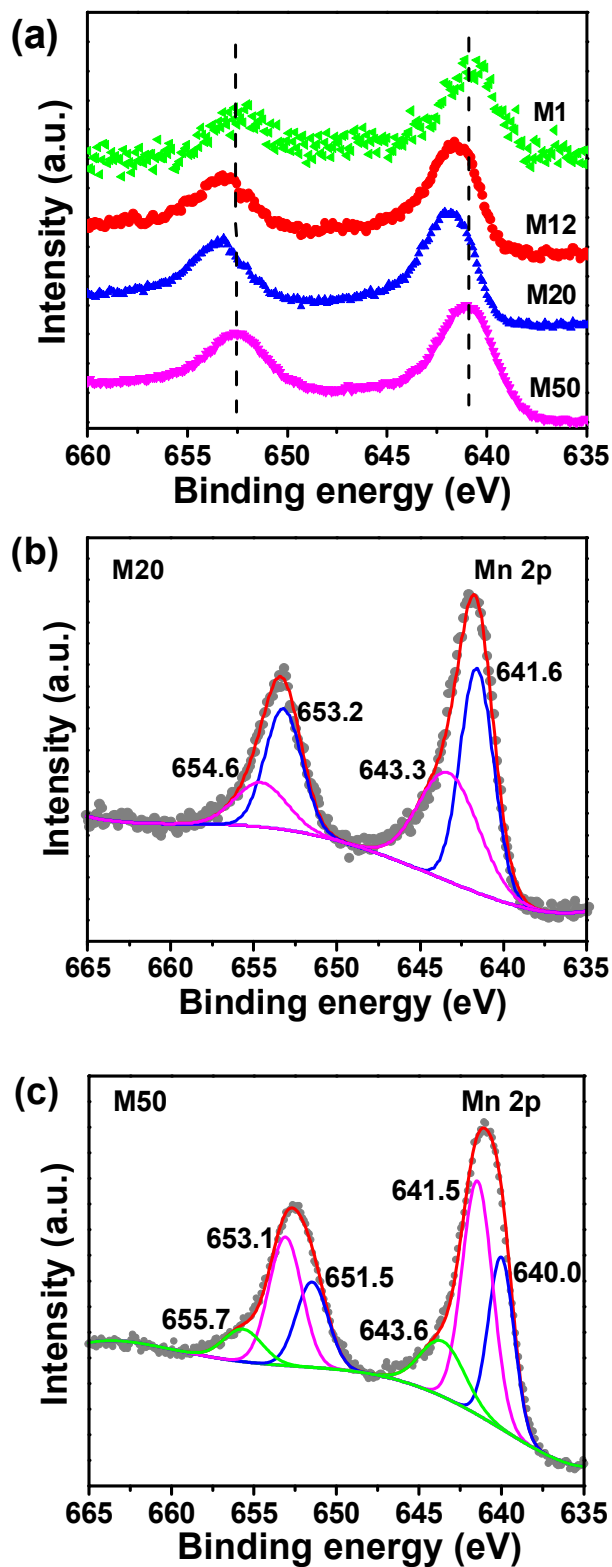
Figure 3 EDX determined Mn/Ti ratios vs. nominal doping levels.

Figure 4 Diffuse reflection absorption spectrum of Mn-TiO$_2$ powders with different levels of Mn incorporation.
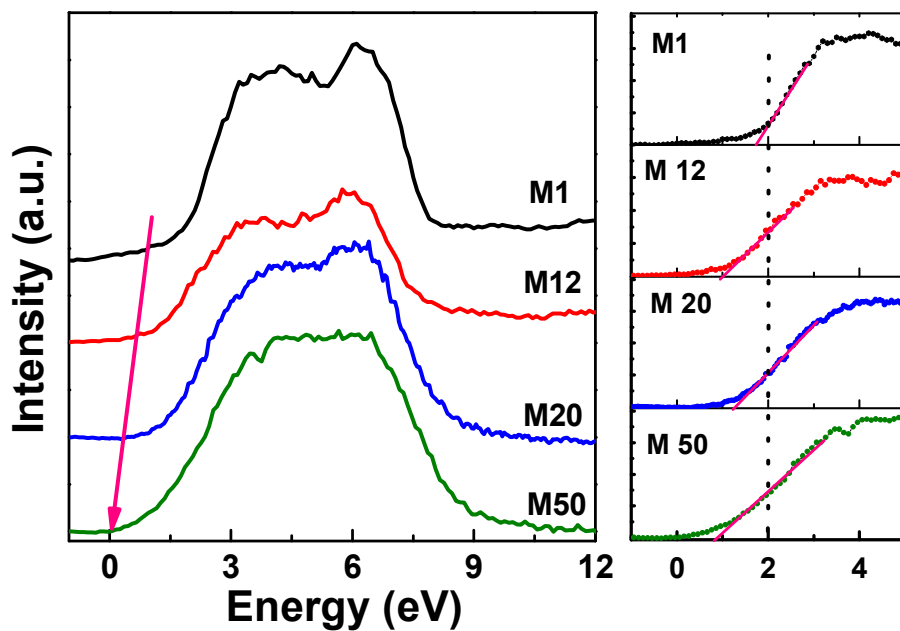
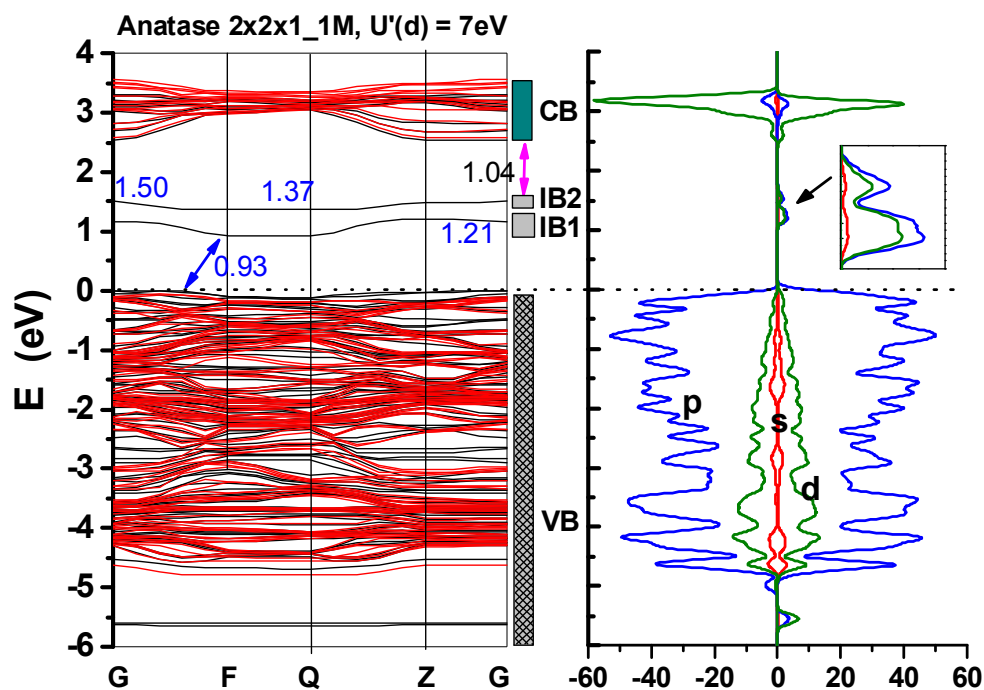**Figure 5** High-resolution XPS spectra of Ti 2p in samples of different Mn levels.

Figure 6 High-resolution XPS spectra of (a) Mn 2p. (b) Deconvoluted peaks of Mn 2p from (b) M12, and (c) M50.
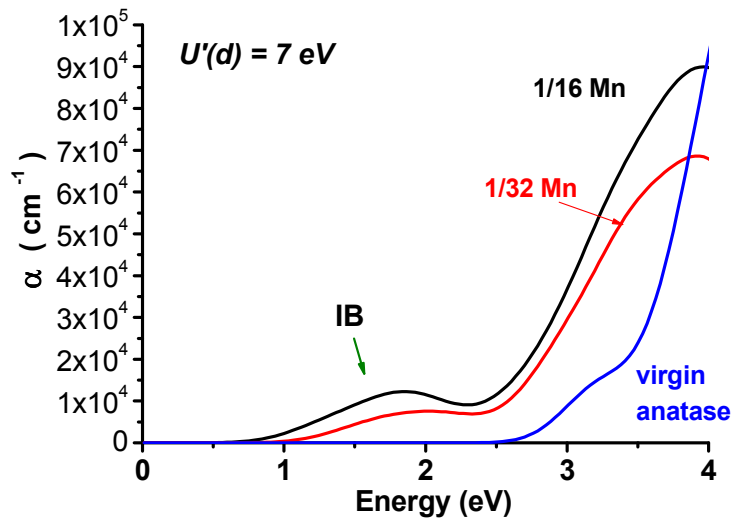
Figure 7 (a) Ti $L_{3,2}$-edge and (b) Mn $L_{3,2}$-edge XANES spectra from Mn-TiO$_2$ with various doping levels. (c) Calculated EELS L_3 edge spectrum of Mn-TiO$_2$ with various doping levels with MnO$_2$ having the anatase structure.
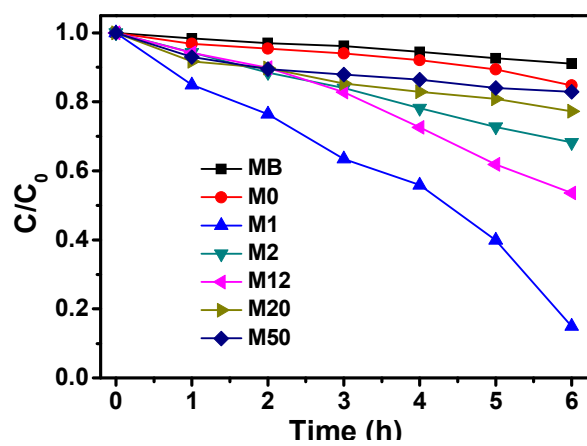
Figure 8 VBXPS spectra of Mn-TiO$_2$ nanoparticles, with an arrow-headed line guiding the evident elevation in the VBM due to Mn doping. The right panel shows the near edge part of the spectra, with the edge positions indicated by the intercepts of the slopes on the energy axis.

Figure 9 Spin polarized band structures (left) and corresponding partial density of states (PDOS, right) for a 2×2×1 anatase supercell containing a substitutional Mn atom. Note from the enlarged inset on the PDOS figure that the IBs are attributed mainly to the O 2p and Mn 3d orbitals. The corresponding Mn/(Ti +Mn) is 6.25%.

Figure 10 DFT + U calculated optical spectra showing the effects of substitutional Mn doping. A Gaussian smearing of 0.5 eV is applied to account for a virtual instrumental resolution.

Figure 11 Photodegradation of methylene blue by TiO$_2$ powder under visible light.